



# Porous activated carbon derived from Chinese-chive for high energy hybrid lithium-ion capacitor

Qun Lu, Bing Lu, Manfang Chen, Xianyou Wang\*, Ting Xing, Meihong Liu, Xingyan Wang

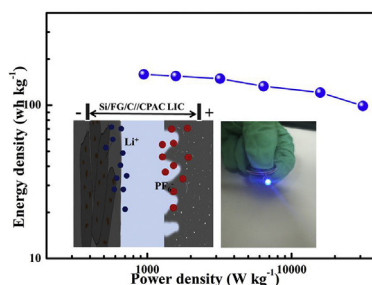
National Base for International Science & Technology Cooperation, National Local Joint Engineering Laboratory for Key Materials of New Energy Storage Battery, Hunan Province Key Laboratory of Electrochemical Energy Storage and Conversion, School of Chemistry, Xiangtan University, Xiangtan, 411105, China

## HIGHLIGHTS

- Biomass-derived activated carbon is prepared via a two-step process utilizing Chinese-chives as carbon precursor.
- The CPAC-5 shows an extremely high specific surface area ( $3011 \text{ m}^2 \text{ g}^{-1}$ ) and relatively applicable pore volume ( $2.6 \text{ m}^3 \text{ g}^{-1}$ ).
- The CPAC-5 displays excellent capacitive performance, good rate capability and capacity retention in organic electrolyte.
- The hybrid Si/FG/C//CPAC system reveals a high energy density of  $99 \text{ Wh kg}^{-1}$  even at a high power density of  $31235 \text{ W kg}^{-1}$ .
- The hybrid Si/FG/C//CPAC system reveals excellent cycle stability with 80% capacity retention rate after 8000 cycles at  $1 \text{ A g}^{-1}$ .

## GRAPHICAL ABSTRACT

Preparation of CPAC and fabrication of Si/FG/C//CPAC hybrid LIC.



## ARTICLE INFO

### Keywords:

Biomass-derived porous carbon  
Chinese-chives  
Electric double-layer capacitor  
Lithium ion battery  
Hybrid lithium-ion capacitor

## ABSTRACT

Lithium-ion capacitor is a hybrid electrochemical energy storage device, which combines the intercalation mechanism of lithium ion battery with the cathode of electric double-layer capacitor. To improve the energy density of hybrid Lithium-ion capacitor, a high-performance ion adsorption cathode is essential. Herein the porous activated carbon for using as cathode of hybrid Lithium-ion capacitor has been prepared through a two-step fabrication process in which naturally Chinese-chives are used as biomass carbon precursor. The biomass-derived porous carbon exhibits an extremely high specific surface area ( $3011 \text{ m}^2 \text{ g}^{-1}$ ) and relatively applicable pore volume ( $2.6 \text{ m}^3 \text{ g}^{-1}$ ). Besides, it displays excellent capacitive performance with specific capacity of  $124 \text{ mAh g}^{-1}$  at a current density of  $0.3 \text{ A g}^{-1}$ , good rate capability and outstanding cycling stability in organic electrolyte. The hybrid Lithium-ion capacitor is assembled using biomass-derived porous carbon as cathode material and the silicon/flake graphite/carbon nanocomposite as anode material. The hybrid device shows a high energy density of  $159 \text{ Wh kg}^{-1}$  at  $945 \text{ W kg}^{-1}$  and outstanding cycle stability (with 80% capacity retention rate after 8000 cycles at  $1 \text{ A g}^{-1}$ ).

\* Corresponding author.

E-mail addresses: [xywang@xtu.edu.cn](mailto:xywang@xtu.edu.cn) (X. Wang), [xywangxtu@xtu.edu.cn](mailto:xywangxtu@xtu.edu.cn) (X. Wang).

<https://doi.org/10.1016/j.jpowsour.2018.07.062>

Received 9 March 2018; Received in revised form 12 June 2018; Accepted 15 July 2018

Available online 19 July 2018

0378-7753/ © 2018 Elsevier B.V. All rights reserved.

## 1. Introduction

The depletion of fossil fuels and the serious deterioration of the global environment have attracted more and more attention and bring a good opportunity for the development of new renewable energy along with energy storage and conversion devices [1,2]. Besides lithium-ion batteries (LIBs) for energy-based devices, supercapacitors (SCs) are considered as a promising system for power-based applications, which possess the advantages of high power density, good rate capability, long cycle life ( $> 10^5$  cycles) and environmental friendliness, etc. [3,4]. However, SCs bear the main defect of low energy density compared with LIBs, which greatly limits its application. In order to overcome the shortcomings of low energy density of SCs and low power density of LIBs, a newly emerged hybrid electrochemical energy storage device called lithium-ion capacitor (LIC) attracts attention of many researchers due to its high energy/power ratio. The energy density of the package LIC with  $20 \text{ Wh kg}^{-1}$  is four times higher than that of EDLC, which is five times lower than that of the lithium ion battery. The power density has been proved to match that of EDLCs able to fully discharge in a few seconds with a double layer capacitor [5]. In general, the hybrid LIC system consists of a SC-type cathode and LIB-type anode, in which the cathode is mainly a high surface area carbonaceous electrode via sorption of ions and the anode is prepared by LIB materials via Li-ion insertion/intercalation [6,7].

Obviously, the cathode and anode materials are really important to the development of LICs. So far, some electrode materials of LIBs, such as  $\text{Li}_4\text{Ti}_5\text{O}_{12}$  [8],  $\text{TiO}_2$  [9],  $\text{V}_2\text{O}_5$  [10], Si [11], have been employed as anodes of hybrid LICs, of which Si possesses the high theoretical capacity and properly low working potential versus  $\text{Li/Li}^+$ . Based on the above considerations and our previous work, the hierarchical silicon/flake graphite/carbon (Si/FG/C) composite [12] is used as anode material of hybrid LIC, which possesses the high specific capacity ( $634 \text{ mAh g}^{-1}$  at 0.2C) for Li-ion storage along with excellent cyclic stability and can provide higher energy density. Furthermore, the Si/FG/C composite was prepared via a scalable and simple synthetic method using Photovoltaic monocrystalline silicon as silicon source that has the advantages of high purity, environment-friendly, low-priced and sufficient resource for large-scale preparation.

Based on the fact of high capacity of anode material, the energy and power density of hybrid LIC system mainly depends on the cathode part due to the asymmetrical structure and the huge difference in the ratio of the cathode and anode specific capacity. Hence, it is necessary to develop the new cathode material and improve the electrochemical performance of hybrid LIC. Generally, A wide variety of carbon materials have been extensively used as cathode material for LICs due to their large specific surface area, high conductivity and controllable meso-/microporosity, which are related to ultimate power and energy storage capacity [13,14]. Among them, biomass-derived carbon is attracting more and more attention as electrode materials for energy storage devices due to their tunable chemical/physical properties, eco-friendliness, rich resources and high economic value [15,16]. In our group, a lot of works on porous carbon materials such as carbon aerogel (CA) [17], carbide-derived carbon (CDC) [18], ordered mesoporous carbon (OMC) [19] as well as the biomass-derived activated carbon [20] as the electrode materials of the symmetric supercapacitors have been extensively studied, of which biomass-derived activated carbons derived from lotus seedpod shells [21] and lotus plumule [22] are used for energy storage of lithium sulfur batteries. Herein the biomass-derived activated carbon has been successfully prepared via a two-step process utilizing agricultural Chinese-chives as a new carbon precursor. The Chinese-chives have many advantages of low cost, short growth cycle, abundant and industrial large-scale production, which should be a promising carbon precursor for the production of activated carbon. In addition, as far as we know, there is no report of the use about Chinese-chives as a biomass precursor to synthesize porous carbon. The obtained biomass-derived carbon used as cathode materials for hybrid LIC

has a narrow micro-to meso-pore distribution and shows a high specific surface area of up to  $3011 \text{ m}^2 \text{ g}^{-1}$  and suitable pore volume of  $2.6 \text{ m}^3 \text{ g}^{-1}$ , of which abundant micropores provide sufficient sites for charge separation and mesopores serve as ion-diffusion channels to promote ion transport and enhance the ion storage in organic electrolyte, resulting in good rate capability and high specific capacity [23,24].

The hybrid LIC device (Si/FG/C//CPAC) composing of Si/FG/C composite as anode and biomass-derived activated carbon as cathode exhibit high energy density of  $159 \text{ Wh kg}^{-1}$  at power density of  $945 \text{ W kg}^{-1}$ , and the energy density still retains  $99 \text{ Wh kg}^{-1}$  even at power density of  $31235 \text{ W kg}^{-1}$ . Consequently, the hybrid device is not only low cost, environmentally friendly, but also excellent in electrochemical performance. This work shows the possibility of a harmonious coexistence between high energy density and high power density, and provides a new strategy for commercial large-scale production.

## 2. Experimental section

### 2.1. Synthesis of Chinese-chives derived porous activated carbon (CPAC)

The Chinese-chives derived porous activated carbon (CPAC) was prepared by a two-step process as presented in Scheme 1. At first, fresh Chinese-chives were washed with distilled water and alcohol many times and dried off at  $80^\circ\text{C}$  for 24 h. Then, the treated Chinese-chives were cut and grinded into small pieces. The treated Chinese-chives were carbonized under  $\text{N}_2$  flow at  $800^\circ\text{C}$  for 5 h with a rate of  $5^\circ\text{C min}^{-1}$ . After that, the carbonized product was immersed in 5 wt% HCl for 2 h at stirring constantly and subsequently rinsed with water, collected by filtration, dried at  $80^\circ\text{C}$  for 12 h. Afterwards, the as-prepared CPAC were further activated by KOH with mass ratio of 1:3 and 1:5. All the samples were activated at  $900^\circ\text{C}$  for 1 h. At last, the product was washed with 5 wt% HCl solution and water to neutrality. Accordingly, the CPAC products were denoted as CPAC-3, CPAC-5, respectively.

### 2.2. Preparation of silicon/flake graphite/carbon (Si/FG/C) composite

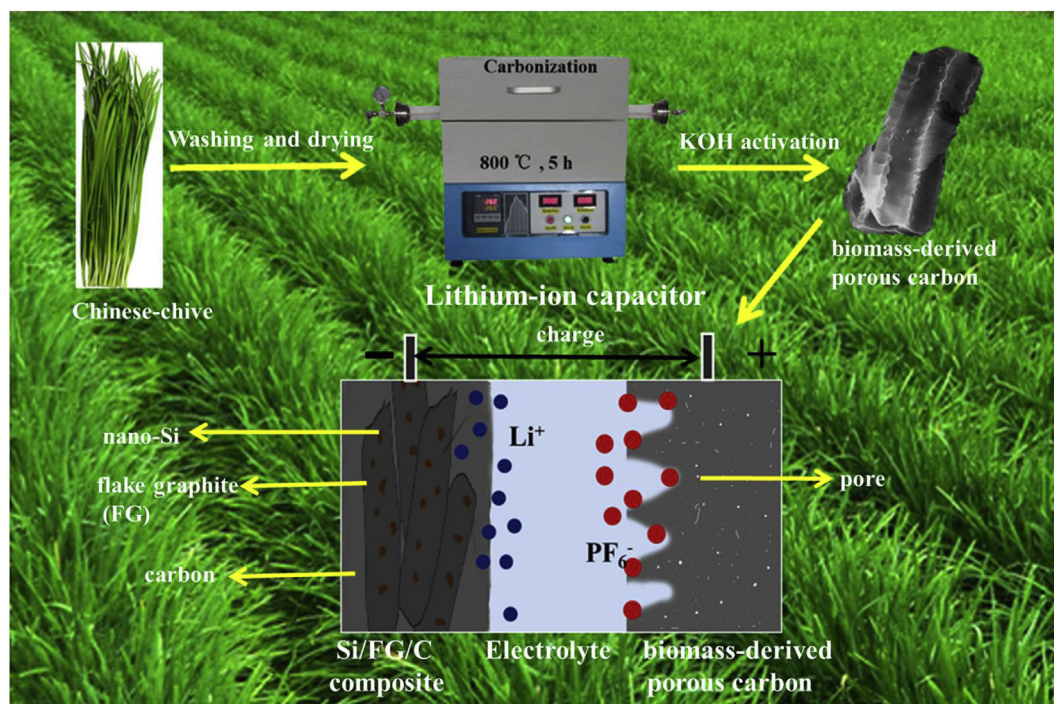
The silicon/flake graphite/carbon (Si/FG/C) composite was prepared through a simple and feasible high temperature calcination method using photovoltaic monocrystalline silicon waste as silicon source based on our previous report [12].

### 2.3. Chemical analysis and textural characterization

The morphologies and texture of the CPAC were characterized with scanning electron microscopy (SEM, Quanta FEG 250, FEI) and transmission electron microscopy (TEM, JEM-2100F, JEOL). Raman spectra were recorded on a LabRAM HR800 Raman spectrometer. X-ray diffraction (XRD) data were used to observe crystal structure of the CPAC using an X-ray diffractometer (Bruker AXS D8, Bruker AXS GmbH, Germany), equipped with Cu K $\alpha$  radiation ( $\lambda = 0.154178 \text{ nm}$ ). The textural properties of CPAC were characterized via  $\text{N}_2$  sorption measurements at  $77.3 \text{ K}$  (JW-BK112). The X-ray photoelectron spectroscopy (XPS) analysis was performed on a Thermo fisher Scientific K-Alpha<sup>+</sup> spectrometer with Al K $\alpha$  ( $1486.6 \text{ eV}$ ) as the X-ray source. The specific surface area SSA was obtained by Brunauer-Emmett-Teller (BET) method. The pore size distribution (PSD) was calculated based on the Barrett-Joyner-Halenda (BJH) model.

### 2.4. Electrochemical testing and electrochemical fabrication of half-cell and LIC (Si/FG/C//CPAC)

A typical homogeneous slurry containing the 80 wt% CPAC active material, 10 wt% acetylene black and 10 wt% Na-Alginate binder in deionized water was used to fabricate the CPAC electrode material, and then painted onto the Al foil. Si/FG/C-based electrodes material were



**Scheme 1.** Schematic illustration for synthesis procedure of CPAC and fabrication of Si/FG/C//CPAC hybrid LIC.

prepared by the mixture made up of 70 wt% Si/FG/C active material, 20 wt% acetylene black and 10 wt% polyvinylidene fluoride (PVDF), which employed the N-methyl-2-pyrrolidone (NMP) as solvent and then coated onto Cu foil. The prepared electrodes subsequently were dried at 80 °C for 12 h under vacuum and then pressed under a pressure of 12 MPa for 60 s. CPAC and Si/FG/C composite samples were firstly examined as anode and cathode materials in the half-cell system with Li metal foil as counter and reference electrodes, a porous polypropylene based membrane (Celgard) as the separator and 1 mol L<sup>-1</sup> LiPF<sub>6</sub> in ethylene carbonate and dimethyl carbonate (EC:DEC = 1:1) as the electrolyte in coin cells. Hybrid LICs were fabricated with CPAC as the cathode material and Si/FG/C composite as the anode material in the same electrolyte as shown in Scheme 1, and the mass ratio of CPAC to Si/FG/C composite was 2:1. All the coin cells were assembled in the glove box with oxygen content less than 1 ppm. Finally, the cells were aged for 12 h before the measurements.

All the electrochemical tests were carried out at normal temperature. The voltage range of Si/FG/C composite electrode was 0.01 V–1.5 V. The CPAC electrodes and the hybrid LIC were measured at the same voltage range of 2.0 V–4.5 V. The energy density and power density were calculated on the basis of the total mass of the active material on the anode and cathode. Cyclic voltammetry (CV) and electrochemical impedance spectroscopy (EIS, frequency ranging from 10<sup>5</sup> to 10<sup>-2</sup> Hz with amplitude of 5 mV) of supercapacitors were conducted on an electrochemical workstation (VersaSTAT3, Princeton Applied Research, USA). The galvanostatic charge/discharge (GCD) and cycle life was measured by test station (Arbin, BT2000, USA).

### 3. Results and discussion

The XRD patterns of CPAC, CPAC-3 and CPAC-5 are shown in Fig. 1a. It can be observed that an inconspicuous humps diffraction peak locates at  $2\theta = \sim 43^\circ$ , which is attributed to a superposition of the graphitic (100) planes and a broad diffraction peak at  $2\theta = \sim 24^\circ$  corresponding to the graphitic (002) reflection for all the samples [25]. Obviously, comparing with CPAC, the much weaker and broader (002) peak of CPAC-3 and CPAC-5 proposes a wider spacing between aromatic layers, indicating that the activation of KOH leads to the fracture

of the domain and the random distribution of graphene sheets in the carbon structure as well as the increase of disordered structure [26]. As shown in Fig. 1b, the structure of all CPAC samples is studied by Raman spectra. It is noticed that the spectra of all CPAC samples contain two strong peaks at 1350 and 1585 cm<sup>-1</sup>, which are attributable to the D and G bands, respectively. The disordered carbon represented by D and G bands is graphitized carbon. The intensity ratio of D/G band expresses the atomic ratio of sp<sup>3</sup>/sp<sup>2</sup> carbons, which can be used to indicate the degree of graphitization [27]. The I<sub>D</sub>/I<sub>G</sub> intensity ratio of CPAC, CPAC-3 and CPAC-5 is determined to be 1.01, 1.03 and 1.08, respectively. Apparently, there is a slight increase in the D/G band intensity ratio of all CPAC samples with the increase of activation ratio of KOH/CPAC, indicating that the activation of KOH destroys a part of the graphite structure.

The XPS is used to evaluate the chemical identities of the heteroatoms in the biomass activated carbon and further analyze the nature and amount of functional groups of the CPAC-5. The XPS survey spectrum and typical C1s, O1s and N1s spectra of the synthesized carbon (CPAC-5) are presented in Fig. 2. As shown in Fig. 2a, there are obvious N1s and O1s peaks which can be observed in the XPS spectra. Based on the results of XPS, the N and O content in CPAC-5 are 4.00 and 12.54 wt%, respectively. The Fig. 2b is the high-resolution C1s spectrum of CPAC-5, which can be deconvoluted into four individual component peaks corresponding to C-C (284.7 eV), C-O (286 eV) and C=O (288.6 eV) [28]. The N1s peak is mainly composed of pyrrolic nitrogen at 400.1 eV (N-5), and pyridinic nitrogen at 398.7 eV (N-6) together with small amount of N-oxides (401.4 eV). The O1s peak is dominated by C-O bond at 532 eV and carbonyl carbon (C=O, 533.5 eV) [29,30]. The above results show that the N and O atoms as electron-withdrawing atoms in CPAC-5 sample change the nearby electronic structure and possess highly activity, and thus these groups can improve the wettability and produce a big pseudocapacitance.

In order to characterize the morphology and microstructure of Chinese-chives derived porous activated carbon, the representative SEM and TEM images of CPAC-5 are presented in Fig. 3. It can be easily observed from the inset in Fig. 3a that CPAC-5 has basically blocky and hollow tubular structure before grinding that possibly inherits from that of Chinese-chives. CPAC-5 became small irregular bulk appearance



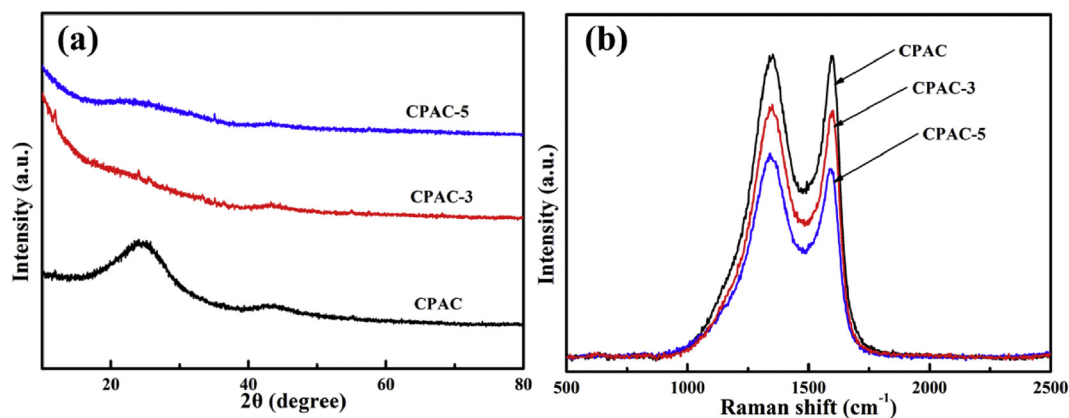


Fig. 1. (a) XRD spectra and (b) Raman spectra of all CPACs samples.

after grinding as presented in Fig. 3a. The porous structure was further studied by TEM technique. It can be seen clearly from Fig. 3b that the CPAC-5 exhibits abundant micro- or meso-pores structure, of which the bright part corresponds to the pores or and curved passages that can effectively promote the fast penetration of electrolyte into the pores. The abundant pore structure is derived from KOH activation and emission of small gaseous molecules such as  $H_2O$ ,  $CO$ ,  $CO_2$  during carbonization. Fig. 3c further demonstrates that the CPAC-5 with porous structure has been successfully produced, which is favorable for the transmission of electrolyte ions. Moreover, from the high-resolution TEM (HRTEM) image in Fig. 3d, an interlayer spacing of about 0.337 nm is estimated, which is in accord with the graphite (002) spacing and it will be propitious to the enhancement of conductivity.

To determine the specific surface area and texture and size of the pore, the  $N_2$  adsorption/desorption isotherms and pore size distribution curves for CPAC, CPAC-3 and CPAC-5 are presented in Fig. 4. As shown

in Fig. 4a, the isotherms of CPAC, CPAC-3 and CPAC-5 are a combination of type I and type IV according to IUPAC classification, thus indicating that three samples are made up of micropore and mesopore, which are beneficial for electrolyte ion transfer [31]. The isotherms of all samples show the sharp increase in the early stage ( $P/P_0 < 0.05$ ), which are ascribed to micropore. Usually, the micropore is generated by emission of small gaseous molecules such as  $H_2O$ ,  $CO$ ,  $CO_2$  during the carbonization process; the inconspicuous hysteresis loops for CPAC-3 and hysteresis loops for CPAC-5 at medium relative pressure can be interpreted as the capillary condensation in the mesopores [32], while hysteresis loop tails of CPAC at high relative pressure region ( $P/P_0 > 0.95$ ) indicate the existence of macropores [33].

The pore size distributions of all the samples are illustrated in Fig. 4b. Usually, according to IUPAC standard the pores can be divided into three types: namely, macropore ( $> 50$  nm), mesopore (2–50 nm) and micropore ( $< 2$  nm). As presented in Fig. 4b, the pore size

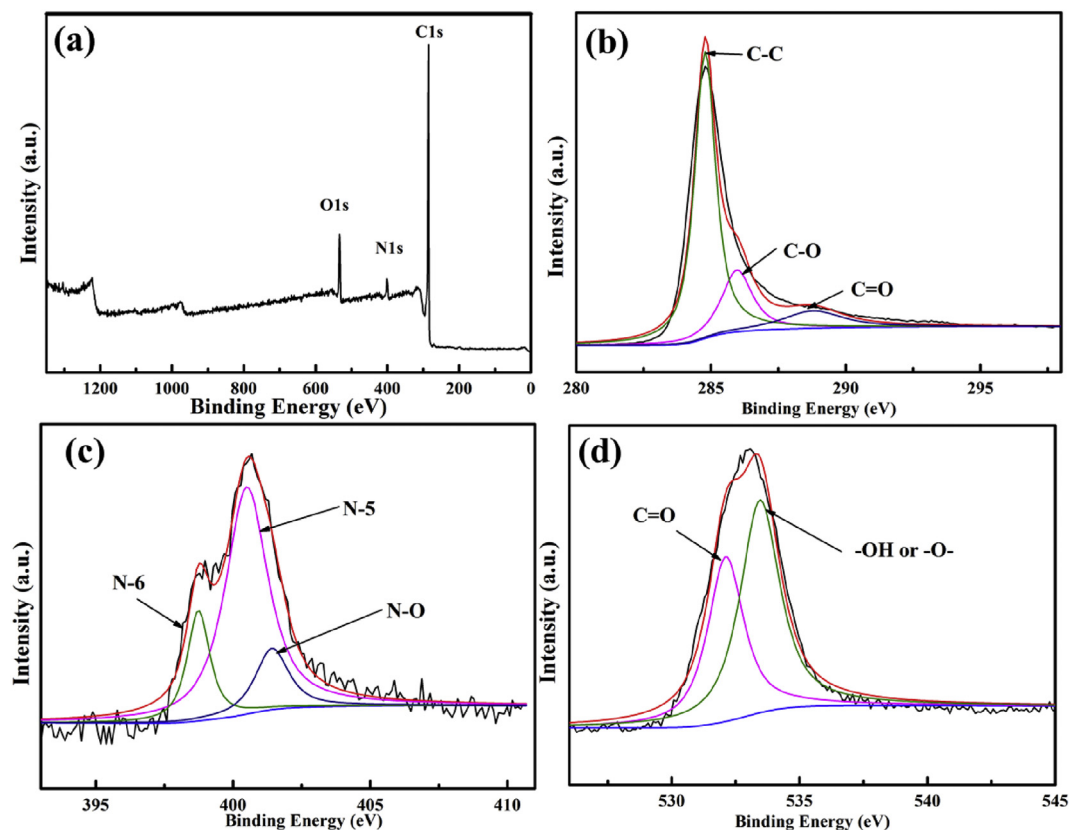


Fig. 2. XPS spectra of the CPAC-5 sample: (a) survey spectrum; (b) C1s; (b) N1s and (d) O1s.

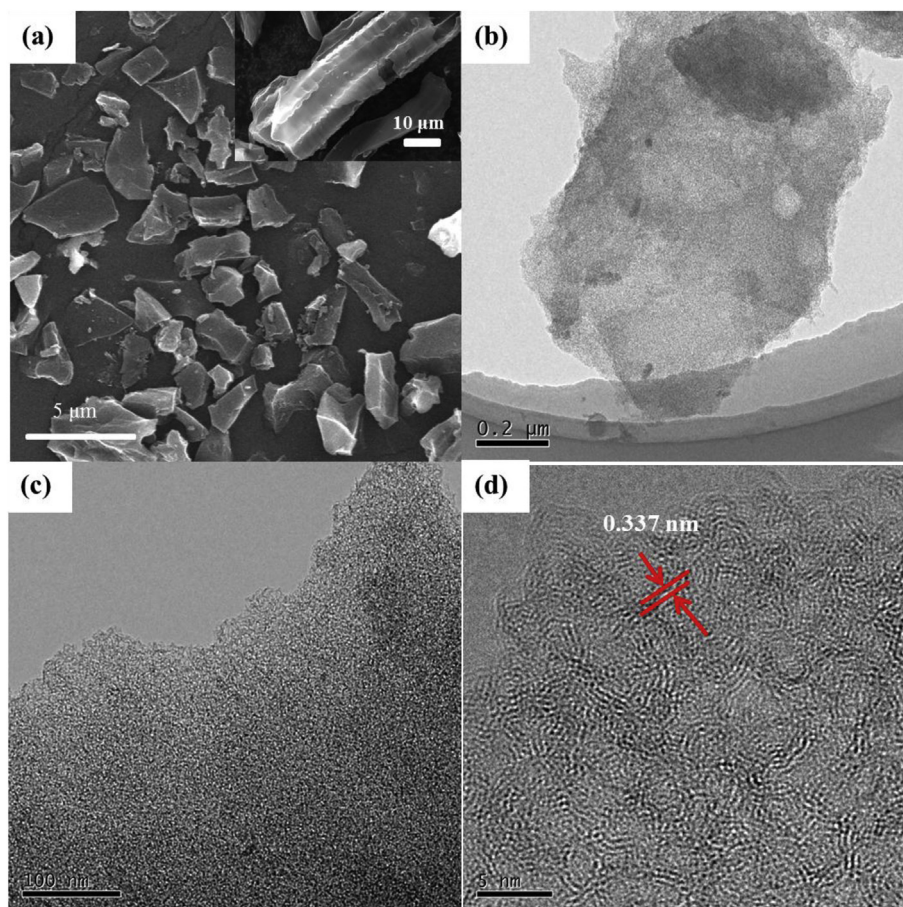


Fig. 3. (a) SEM image of CPAC-5 (the inset shows SEM image of CPAC-5 before grinding), (b) and (c) TEM image of CPAC-5, and (d) HRTEM image of CPAC-5.

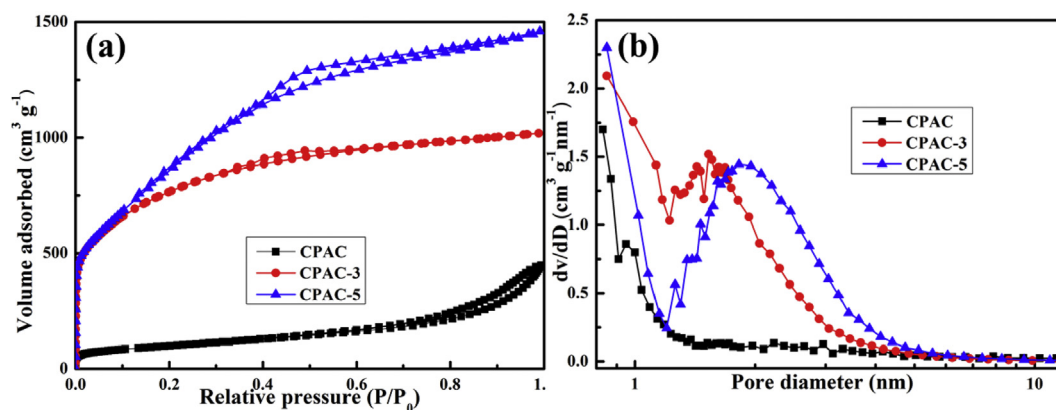


Fig. 4. (a) Nitrogen adsorption/desorption isotherms at 77 K and (b) pore-size distribution of all CPACs.

Table 1

Textural parameters of all the samples obtained from nitrogen adsorption-desorption isotherms.

Samples	BET surface area ( $\text{m}^2 \text{g}^{-1}$ )	Pore volume ( $\text{cm}^3 \text{g}^{-1}$ )	Micropore volume ( $\text{cm}^3 \text{g}^{-1}$ )	BET average pore size (nm)
CPAC	515	0.30	0.10	1.92
CPAC-3	2672	1.58	1.07	2.37
CPAC-5	3011	2.26	1.14	2.77

distribution of all the samples is between 0.8 and 5 nm, which indicates the formation of micropores and mesoporous pores. Besides, as the weight ration of KOH/CPAC increases, the pore size distribution is

widened in the range of mesopore, indicating that the size is larger and the slightly larger size mesopores is formed. The results reveal that KOH activation significantly affects the pore size distribution. With the increase of the weight ratio of KOH/CPAC, the pore size of the prepared carbon samples is also increased. This phenomenon is related to the KOH activation which contributes to the formation of micropores and the expansion of the original micropores into mesoporous pores. The KOH activation mechanism is usually considered as follow [34]:



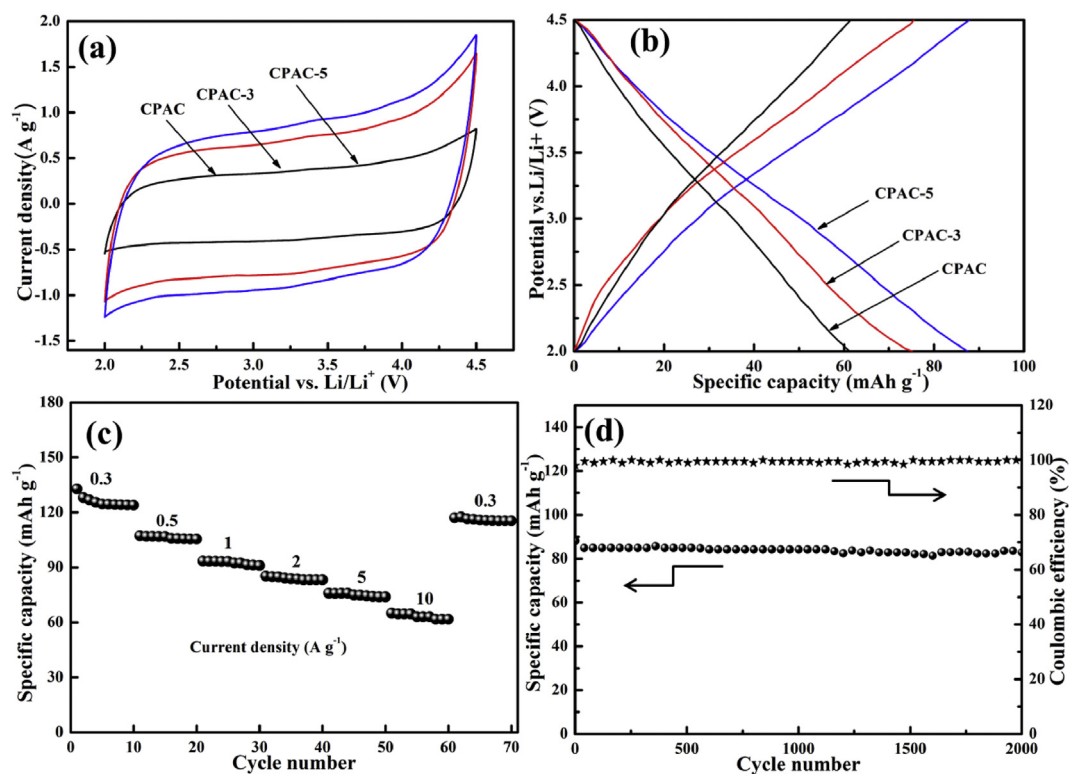


Fig. 5. (a) CV diagram of all CPACs at scan rate of  $5 \text{ mV s}^{-1}$ , (b) GCD profile of all CPACs at current densities of  $1 \text{ A g}^{-1}$ , (c) Rate performance of the CPAC-5, and (d) Cycling performance of CPAC-5 at current densities of  $1 \text{ A g}^{-1}$ .

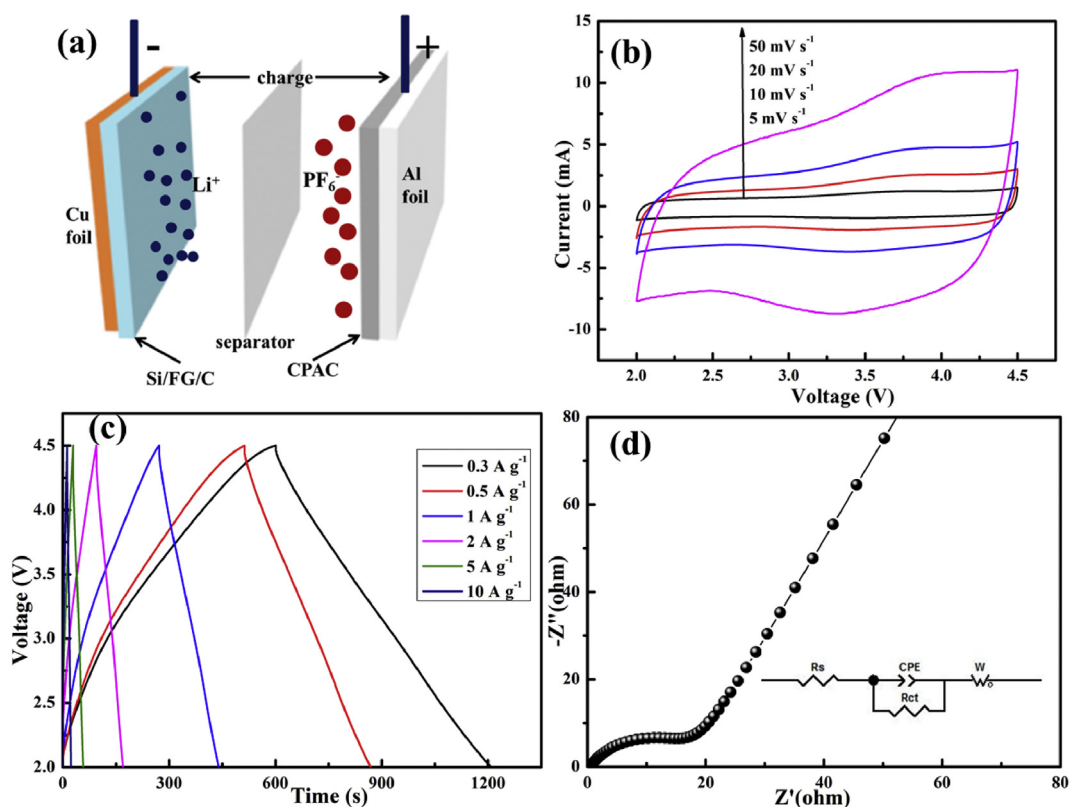
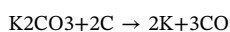
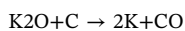


Fig. 6. Mechanism and electrochemical performances of the LIC. (a) Schematic illustration of the assembled structure, (b) CV curves at various scan rates, (c) GCD profile at different current densities, (d) The Nyquist plots and corresponding equivalent circuit diagram.



(4)



(5)

More detailed information about the textural properties of all samples is listed in Table 1. As shown in Table 1, the measured BET



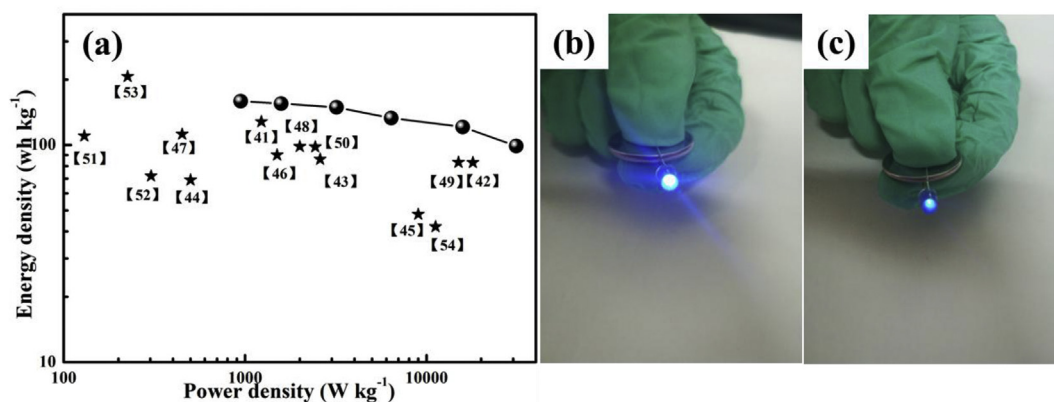


Fig. 7. (a) Ragone plot in comparison with literature, (b) A picture showing that LIC can lighten up LED indicator at start, (c) Images of the blue LED powered by the 1 h charged hybrid LIC. (For interpretation of the references to colour in this figure legend, the reader is referred to the Web version of this article.)

Table 2

Comparative representation of the electrochemical performances with recently published Li-ion hybrid capacitors in organic system.

Hybrid System (anode//cathode)	Voltage window	energy density (Wh kg <sup>-1</sup> )	power density (W kg <sup>-1</sup> )	Ref.
B-Si/SiO <sub>2</sub> /C//AC	2.0–4.5	128	1229	[41]
MnO/CNS//CNS	0.0–4.0	83	18000	[42]
Fe <sub>3</sub> O <sub>4</sub> graphene//3D graphene	1.0–4.0	86	2587	[43]
LTO//AC	1.0–3.0	69	~500	[44]
soft carbon//AC	0.0–4.0	48	9000	[45]
3D-MnO//CNS	1.0–4.0	90	1500	[46]
TiC//PHPNC	0.0–4.5	112	450	[47]
NbN//NG	2.0–4.0	98.4	2000	[48]
MnO@GNS//HNC	1.0–4.0	83.25	15000	[49]
DC//MG (NIC) <sup>a</sup>	0.0–4.2	98	2432	[50]
Li <sub>3</sub> VO <sub>4</sub> //CFs	0.0–3.8	110	130	[51]
TiO <sub>2</sub> @EEG//EEG	0.0–3.0	72	303	[52]
ANCS//ANCS	0.0–4.5	206.7	225	[53]
AMC//PdCS	0.5–4.0	42	11200	[54]
Si/FG/C//CPAC	2.0–4.5	159	945	this work
		99	31235	

<sup>a</sup> The NIC is the abbreviation of sodium ion capacitor.

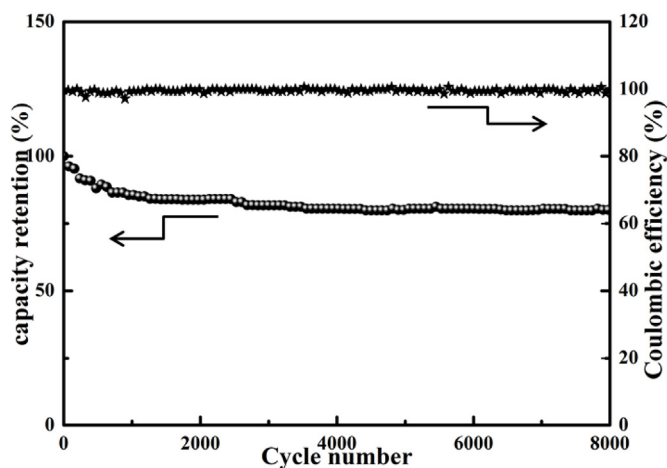


Fig. 8. Cycling performance of the LIC at 1 A g<sup>-1</sup> and the coulombic efficiency of LIC.

specific surface areas are 515, 2672 and 3011 m<sup>2</sup> g<sup>-1</sup> with the pore volumes are 0.30, 1.58 and 2.26 cm<sup>3</sup> g<sup>-1</sup> for CPAC, CPAC-3 and CPAC-5, respectively. Obviously, CPAC-5 exhibits the highest specific surface area and largest micropore volume among all samples, which is related

to the adding amount of activator KOH. Generally speaking, the activator KOH can corrode carbon material in the activation process to form a porous structure, and thus leading to an increase of the specific surface area and enlargement of the pore sizes [32].

The electrochemical performance of all CPAC electrode using as coin cell in a Li half-cell system are evaluated by CV and GCD in the voltage window of 2.0–4.5 V versus Li/Li<sup>+</sup>. Fig. 5a shows the CV profiles of all CPACs at 5 mV s<sup>-1</sup>, which present quasi-rectangular shapes with slight humps indicating the capacitive behavior and subordinate pseudocapacitance derived from the heteroatom in biomass carbon [35,36]. Fig. 5b is GCD curves of all samples. They display nearly linear relation, which indicates the capacitive behavior with the anion (PF<sub>6</sub><sup>-</sup>) adsorption/desorption over the surface. Obviously, CPAC-5 exhibits the highest specific capacity among all samples. The specific capacities of CPAC-5, CPAC-3 and CPAC at 1 A g<sup>-1</sup> is 88, 75, 62 mAh g<sup>-1</sup>, respectively. It can be known from the Fig. 5c that the CPAC-5 reveals a high specific capacity of 135 mAh g<sup>-1</sup> at 0.3 A g<sup>-1</sup> and still retains 65 mAh g<sup>-1</sup> even at the current densities of 10 A g<sup>-1</sup>, showing an excellent stability and a good rate capability. Furthermore, CPAC-5 presents a good cycling stability and outstanding coulombic efficiency as shown in Fig. 5d. CPAC-5 shows the excellent capacity retention of about 94% after 2000 cycles. The coulombic efficiency of CPAC-5 is almost 100% during the whole charge/discharge cycling process, which demonstrates that it possesses the good reversibility and excellent electrochemical stability.

Fig. 5 is schematic mechanism and electrochemical performances of the LIC. The hybrid LIC is assembled using pre-lithidated Si/FG/C nanocomposite as the anode materials and CPAC-5 as the cathode materials in 1 mol L<sup>-1</sup> LiPF<sub>6</sub> dissolved in EC-DMC electrolyte solution (the hybrid LIC denoted as Si/FG/C//CPAC). The detailed work mechanism of Si/FG/C//CPAC in the voltage range of 2.0–4.5 V was shown in Fig. 5a. During the charge process, PF<sub>6</sub><sup>-</sup> ions are accumulated on the interface of CPAC-5 electrode/electrolyte while Li<sup>+</sup> ions in the electrolyte insert into Si/FG/C anode, probably accompanied with the Li adsorption mechanism of carbon matrix. In the discharging process, PF<sub>6</sub><sup>-</sup> ions and Li<sup>+</sup> flee from the CPAC cathode and Si/FG/C anode respectively [37]. Fig. 6b–d shows the electrochemical performances of Si/FG/C//CPAC. The CV curves of Si/FG/C//CPAC shown in Fig. 6b exhibit quasi-rectangular shapes with increasing the scan rate from 5 mV s<sup>-1</sup> to 50 mV s<sup>-1</sup>, and the CV shapes show a little deformation, indicating a good reversibility. Fig. 6c shows the voltage profiles at different current densities. It can be seen slightly deviation from the slope of the straight line, which should be attributed to the overlapping effects of two different energy-storage mechanisms from the cathode (no Faradaic reaction) and anode (Faradaic reaction) [38,39]. Electrochemical impedance spectroscopy (EIS) is further carried out to gain insight into performance of the hybrid LIC. Fig. 6d presents Nyquist

plots of impedance spectra which can be fitted by the equivalent circuit consisting of a bulk solution resistance ( $R_s$ ), a charge-transfer resistance ( $R_{ct}$ ), a constant phase element (CPE) accounting for the electrical double-layer capacitance, and a Warburg resistance ( $W$ ) as shown in inset of Fig. 6d. As being seen from the Fig. 6d, the shape of EIS curves is composed of low-frequency linear parts and high-frequency arc-shaped parts. The Nyquist plot of the Si/FG/C//CPAC hybrid LIC shows a small arc in the high-to-medium frequency region, which is generally ascribed to a relatively low charge transfer resistance in the organic electrolyte [40]. It is worth noting that the hybrid LIC exhibits low internal resistance of  $0.4\ \Omega$ .

Considering that the power density and energy density play a significant part in the evaluation of supercapacitor performance, the Ragone plot (power density vs. energy density) of hybrid LIC is presented in Fig. 7a. The energy and power densities of Si/FG/C//CPAC hybrid LIC can be calculated based on the galvanostatic charge/discharge curves according to Eqs. (6) and (7), respectively [41]:

$$E = \int_{t_1}^{t_2} IV dt \quad (6)$$

$$P = \frac{E}{t_2 - t_1} \quad (7)$$

where  $E$ ,  $V$ ,  $I$ ,  $P$ ,  $t_1$  and  $t_2$  are the energy density ( $\text{Wh kg}^{-1}$ ), voltage (V), constant current density ( $\text{A kg}^{-1}$ ), power density ( $\text{W kg}^{-1}$ ), discharge start and end time (h), respectively. The Si/FG/C//CPAC hybrid LIC exhibits a high energy density of  $159\ \text{Wh kg}^{-1}$  at  $945\ \text{W kg}^{-1}$ , it can still maintain at  $99\ \text{Wh kg}^{-1}$  even at a high power density of  $31235\ \text{W kg}^{-1}$ . Fig. 6b and c is the photos of LIC lighting LED indicator at start and after 1 h. In Fig. 7b and c, a blue round light-emitting diode (LED) with 3 mm diameter in the high working voltage of 2.5 V can be easily lit up by the Si/FG/C//CPAC hybrid device, and even remained bright after 1 h. This physical demonstration further indicated that Si/FG/C//CPAC hybrid LIC is a kind of promising electrochemical energy storage device. Furthermore, Table 2 is comparisons of the currently reported Li-ion hybrid systems with assembled Si/FG/C//CPAC hybrid LIC, such as MnO/CNS//CNS [42], LTO//AC [44], soft carbon//AC [45], 3D-MnO//CNS [46], TiC//PHPNC [47], NbN//NG [48] and so on. Apparently, the Si/FG/C//CPAC hybrid LIC in this work reveals a clear superiority whether at high power density or at low power density.

It is well-known that the cycle life is another key factor for the supercapacitor application. As shown in Fig. 8, the cycle life curves of hybrid LIC coin cell are tested at a current density of  $1\ \text{A g}^{-1}$  for 8000 cycles. It can be seen from Fig. 8 that the capacity of the Si/FG/C//CPAC hybrid LIC decrease rapidly during the initial cycle, which can be ascribed to incompletely permeation of electrolyte in the initial charge/discharge process and irreversible reaction in the process of initial activation as well as the SEI formation. Finally, the capacity retention for the Si/FG/C//CPAC hybrid LIC still remains about 80% after 8000 cycles. Obviously, the hybrid LIC system displays outstanding cycle stability. Consequently, the as-prepared Si/FG/C//CPAC hybrid LIC possesses excellent supercapacitive characteristics, and its raw materials are derived from photovoltaic monocrystalline silicon waste and biomass, so the raw materials are readily available and the cost is low.

#### 4. Conclusions

A hybrid lithium-ion capacitor has been successfully designed by biomass-derived porous carbon cathode and a high-performance Si/FG/C nanocomposite anode. The obtained porous carbon derived from naturally Chinese-chives presents an extremely high specific surface area ( $3011\ \text{m}^2\ \text{g}^{-1}$ ) and relatively suitable pore volume ( $2.6\ \text{m}^3\ \text{g}^{-1}$ ), which is propitious to shuttle and permeation of electrolyte ions, thereby showing an excellent capacitive performance with a specific capacity of  $124\ \text{mAh g}^{-1}$  in organic electrolyte at  $0.3\ \text{A g}^{-1}$  and

capacity retention of 94% after 2000 cycles. The hybrid Si/FG/C//CPAC system reveals a high energy density of  $159\ \text{Wh kg}^{-1}$  at  $945\ \text{W kg}^{-1}$  and outstanding cycle stability with 80% capacity retention rate after 8000 cycles at  $1\ \text{A g}^{-1}$ . Besides, the as-prepared hybrid LIC are both high energy density and beneficial to commercial large-scale production since either abundant resource, low-cost, easy preparation for the cathode material or non-poisonous, low-priced and simple process for anode material. Therefore, the low-cost Si/FG/C//CPAC hybrid LIC is expected to be the advanced next-generation energy storage devices with high-power capabilities in hybrid vehicle systems and flexible wearable devices.

#### Acknowledgments

This work was financially supported by the National Natural Science Foundation of China (Grant Nos. 51072173, 51272221 and 51302239), Specialized Research Fund for the Doctoral Program of Higher Education (Grant Nos. 20134301130001), the Natural Science Foundation of Hunan Province, China (Grant Nos. 13JJ4051).

#### References

- [1] Q. Lu, J.G. Chen, J.Q. Xiao, *Angew. Chem. Int. Ed.* 52 (2013) 1882–1889.
- [2] N.S. Choi, Z. Chen, S.A. Freunberger, D.X. Ji, Y.K. Sun, K. Amine, G. Yushin, L.F. Nazar, J. Cho, P.G. Bruce, *Angew. Chem. Int. Ed.* 51 (2012) 9994–10024.
- [3] F. Wang, X. Wu, X. Yuan, Z. Liu, Y. Zhang, L. Fu, Y. Zhu, Q. Zhou, Y. Wu, W. Huang, *Chem. Soc. Rev.* 46 (2017) 6816–6854.
- [4] Y. Wang, Y. Xia, *Adv. Mater.* 25 (2013) 5336–5342.
- [5] N. Arun, A. Jain, V. Aravindan, S. Jayaraman, W.C. Ling, M.P. Srinivasan, S. Madhavi, *Nanomater. Energy* 12 (2015) 69–75.
- [6] Y. Ma, H. Chang, M. Zhang, Y. Chen, *Adv. Mater.* 27 (2015) 5296–5308.
- [7] V. Aravindan, Y.S. Lee, S. Madhavi, *Adv. Energy Mater.* 7 (2017).
- [8] J.P. Zheng, *J. Electrochem. Soc.* 150 (2003) A484–A492.
- [9] H. Kim, M.Y. Cho, M.H. Kim, K.Y. Park, H. Gwon, Y. Lee, K.C. Roh, K. Kang, *Adv. Energy Mater.* 3 (2013) 1500–1506.
- [10] V. Aravindan, Y.L. Cheah, W.F. Mak, D.G. Wee, B.V.R. Chowdari, S. Madhavi, *ChemPlusChem* 77 (2012) 570–575.
- [11] X. Liu, H.G. Jung, S.O. Kim, H.S. Choi, S. Lee, J.H. Moon, J.K. Lee, *Sci. Rep.* 3 (2013) 3183.
- [12] B. Lu, B. Ma, R. Yu, Q. Lu, S. Cai, M. Chen, Z. Wu, K. Xiang, X. Wang, *Chemistry* 2 (2017) 3479–3489.
- [13] J. Yan, Q. Wang, T. Wei, Z. Fan, *Adv. Energy Mater.* 4 (2014).
- [14] E. Frackowiak, *Phys. Chem. Chem. Phys.* 9 (2007) 1774–1785.
- [15] J. Wang, P. Nie, B. Ding, S. Dong, X. Hao, H. Dou, X. Zhang, *J. Mater. Chem.* 5 (2017) 2411–2428.
- [16] H. Zhu, W. Luo, P.N. Ciesielski, Z. Fang, J.Y. Zhu, G. Henriksson, M.E. Himmel, L. Hu, *Chem. Rev.* 116 (2016) 9305–9374.
- [17] J. Li, X. Wang, Y. Wang, Q. Huang, C. Dai, S. Gamboa, *J. Non-cryst. Solids* 354 (2008) 19–24.
- [18] C. Wu, J. Gao, Q. Zhao, Y. Zhang, Y. Bai, X. Wang, X. Wang, *J. Power Sources* 269 (2014) 818–824.
- [19] J. Gao, X. Wang, Q. Zhao, Y. Zhang, J. Liu, *Electrochim. Acta* 163 (2015) 223–231.
- [20] M. Chen, X. Wang, S. Cai, Z. Ma, P. Song, A.C. Fisher, *J. Mater. Chem.* 4 (2016) 16148–16156.
- [21] M. Chen, S. Jiang, S. Cai, X. Wang, K. Xiang, Z. Ma, P. Song, A.C. Fisher, *Chem. Eng. J.* 313 (2017) 404–414.
- [22] M. Chen, S. Jiang, C. Huang, X. Wang, S. Cai, K. Xiang, Y. Zhang, J. Xue, *ChemSusChem* 10 (2017) 1803–1812.
- [23] S. Dutta, A. Bhaumik, K.C.W. Wu, *Energy Environ. Sci.* 7 (2014) 3574–3592.
- [24] M.H. Sun, S.Z. Huang, L.H. Chen, Y. Li, X.Y. Yang, Z.Y. Yuan, B.L. Su, *Chem. Soc. Rev.* 45 (2016) 3479–3563.
- [25] Q. Zhao, X. Wang, C. Wu, J. Liu, H. Wang, J. Gao, Y. Zhang, H. Shu, *J. Power Sources* (2014) 10–17.
- [26] B. Liu, H. Chen, Y. Gao, H. Li, *Electrochim. Acta* (2016) 93–100.
- [27] D. Zhang, X. Zhang, Y. Chen, P. Yu, C. Wang, Y. Ma, *J. Power Sources* 196 (2011) 5990–5996.
- [28] J. Han, G. Xu, B. Ding, J. Pan, H. Dou, D.R. MacFarlane, *J. Mater. Chem.* 2 (2014) 5352–5357.
- [29] L. Qie, W. Chen, H. Xu, X. Xiong, Y. Jiang, F. Zou, X. Hu, Y. Xin, Z. Zhang, Y. Huang, *Energy Environ. Sci.* 6 (2013) 2497–2504.
- [30] L. Qie, L.X. Yuan, W.X. Zhang, W.M. Chen, Y.H. Huang, *J. Electrochem. Soc.* 159 (2012) A1624–A1629.
- [31] F. Sun, J. Gao, Y. Zhu, X. Pi, L. Wang, X. Liu, Y. Qin, *Sci. Rep.* 7 (2017) 40990.
- [32] K. Karthikeyan, S. Amareesh, S.N. Lee, X. Sun, V. Aravindan, Y.G. Lee, Y.S. Lee, *ChemSusChem* 7 (2014) 1435–1442.
- [33] K. Cho, K. Na, J. Kim, O. Terasaki, R. Ryoo, *Chem. Mater.* 24 (2012) 2733–2738.
- [34] E. Raymundo-Pinero, P. Azais, T. Cacciaguerra, D. Cazorla-Amorós, A. Linares-Solano, F. Béguin, *Carbon* 43 (2005) 786–795.
- [35] J. Niu, R. Shao, M. Liu, J. Liang, Z. Zhang, M. Dou, Y. Huang, F. Wang, *Energy*



- Storage Mater. 12 (2018) 145–152.
- [36] B. Li, F. Dai, Q. Xiao, L. Yang, J. Shen, C. Zhang, M. Cai, *Energy Environ. Sci.* 9 (2016) 102–106.
- [37] H. Wang, Y. Zhang, H. Ang, Y. Zhang, H.T. Tan, Y. Zhang, Y. Guo, J.B. Franklin, X.L. Wu, M. Srinivasan, H.J. Fan, Q. Yan, *Adv. Funct. Mater.* 26 (2016) 3082–3093.
- [38] B. Li, F. Dai, Q. Xiao, L. Yang, J. Shen, C. Zhang, M. Cai, *Adv. Energy Mater.* 6 (2016).
- [39] B. Li, F. Dai, Q. Xiao, L. Yang, J. Shen, C. Zhang, M. Cai, *Environ. Sci.* 9 (2016) 102–106.
- [40] E. Pollak, G. Salitra, V. Baranchugov, D. Aurbach, *J. Phys. Chem. C* 111 (2007) 11437–11444.
- [41] R. Yi, S. Chen, J. Song, M.L. Gordin, A. Manivannan, D. Wang, *Adv. Funct. Mater.* 24 (2014) 7433–7439.
- [42] H. Wang, Z. Xu, Z. Li, K. Cui, J. Ding, A. Kohandehghan, X. Tan, B. Zahiri, B.C. Olsen, C.M.B. Holt, D. Mitlin, *Nano Lett* 14 (2014) 1987–1994.
- [43] F. Zhang, T. Zhang, X. Yang, L. Zhang, K. Leng, Y. Huang, Y. Chen, *Energy Environ. Sci.* 6 (2013) 1623–1632.
- [44] A. Jain, V. Aravindan, S. Jayaraman, P. Kumar, R. Balasubramanian, S. Ramakrishna, S. Madhavi, M. Srinivasan, *Sci. Rep.* 3 (2013) 3002.
- [45] M. Schroeder, M. Winter, S. Passerini, A. Balducci, J. Power Sources 238 (2013) 388–394.
- [46] H. Wang, Z. Xu, Z. Li, K. Cui, J. Ding, A. Kohandehghan, X. Tan, B. Zahiri, B. Olsen, C. Holt, D. Mitlin, *Nano Lett* 14 (2014) 1987–1994.
- [47] H. Wang, Y. Zhang, H. Ang, Y. Zhang, H. Tan, Y. Zhang, Y. Guo, J. Franklin, X. Wu, M. Srinivasan, H. Fan, Q. Yan, *Adv. Funct. Mater.* 26 (2016) 3082–3093.
- [48] M. Liu, L. Zhang, P. Han, X. Han, H. Du, X. Yue, Z. Zhang, H. Zhang, G. Cui, *Part. Syst. Char.* 32 (2015) 1006–1011.
- [49] M. Yang, Y. Zhong, J. Ren, X. Zhou, J. Wei, Z. Zhou, *Adv. Energy Mater.* 5 (2015).
- [50] F. Wang, X. Wang, Z. Chang, X. Wu, X. Liu, L. Fu, Y. Zhu, Y. Wu, W. Huang, *Adv. Mater.* 27 (2015) 6962–6968.
- [51] F. Wang, Z. Liu, X. Yuan, J. Mo, C. Li, L. Fu, Y. Zhu, X. Wu, Y. Wu, *J. Mater. Chem.* 5 (2017) 14922–14929.
- [52] F. Wang, C. Wang, Y. Zhao, Z. Liu, Z. Chang, L. Fu, Y. Zhu, Y. Wu, D. Zhao, *Small* 12 (2016) 6207–6213.
- [53] F. Sun, X. Liu, H.B. Wu, L. Wang, J. Gao, H. Li, Y. Lu, *Nano Lett* 18 (2018) 3368–3376.
- [54] W.S.V. Lee, X. Huang, T.L. Tan, M. Xue, *ACS Appl. Mater. Interfaces* 10 (2018) 1690–1700.